

## Methods

### 1. Electron probe microanalysis (EPMA).

EPMA was carried out at Wuhan Shangpu Analysis Technology Co., Ltd, Wuhan, China, using a JXA-8230 electron microprobe. Point analysis was performed with an accelerating voltage of 15 kV, a beam current of 20 nA and an electron beam size of 3  $\mu\text{m}$ . X-ray maps were acquired with 20 kV accelerating voltage, a 100 nA beam current with a 3  $\mu\text{m}$  spot size and 45-50 ms dwell time. 10 elements (Si, Ti, Al, Fe, Mn, Mg, Na, Ca, K, Cr) were measured for both point analysis and X-ray map analysis. The Ti-in-amphibole thermometry developed by [Liao et al. \(2021\)](#) was applied to calculate the formation temperature of amphibole. This thermometry is applicable for calcium amphibole under conditions that Ti-phases (rutile, ilmenite, or titanite) are present, which is satisfied by our samples shown by the occurrence of Ti-Fe oxides.

**2. Electron backscattered diffraction (EBSD).** EBSD analysis was carried out at the Key Laboratory of Deep-Earth Dynamics of Ministry of Natural Resources, Chinese Academy of Geological Sciences. EBSD data were acquired on a FEI Quanta 450 scanning electron microscope mounted with Nordlys F+ high-speed EBSD detector with the thin section surface inclined at 70° to the incidental beam. Measurements were performed on polished thin sections at an 18.4 mm working distance with an acceleration voltage of 20 kV.

One of each gabbro type (YJ2008–2, YJ2003–1 and YJ2020–1) was selected to carry out small-area EBSD mapping with step sizes of 3–6  $\mu\text{m}$ , for detailed microstructure and deformation mechanism analysis. Other samples (YJ2008–2, YJ2007–5, YJ2002–3 and YJ2012–1) were chosen to carry out large-area EBSD mapping for crystal preferred orientation (CPO) and seismic properties calculation.

EBSD patterns were automatically measured and indexed within Oxford Instruments Aztec software. The raw maps were first filtered in Channel 5 software suite to improve the quality of maps. Noise reduction was performed by removing single pixels that differed more than 10° and replacing zero-resolution points with the orientation of nearest neighbours starting from eight neighbours down to five. Texture component map (TCM), misorientation profile and Schmid factor map were obtained in Channel 5 software suite. Other maps were calculated and plotted using MTEX, a MATLAB toolbox ([Hielscher and Schaeben, 2008](#); [Bachmann et al., 2010](#); [Mainprice et al., 2014](#)) for EBSD data process.

In MTEX v.5.7.0, grains were first constructed by identifying grain boundary once the adjacent pixels have a misorientation angles (defined as the lowest rotation angle between two pixels about a common axis that brings two lattices into parallelism; [Lloyd et al., 1997](#)) larger than 10°. Grains constituted by less than 10 pixels were discarded before the following processes. Subgrain boundaries are plotted where the adjacent pixels have a misorientation angle between 2 and 10°. Pole figures were created by plotting the mean crystallographic orientation of each grain (i.e., one point per grain) on lower hemisphere stereographic projection. Both J-index and M-index were calculated (one point per grain) to quantify the strength of CPOs. Misorientation axes have been determined in crystal coordinate for ranges of misorientation angles of 2–10°. The shape preferred orientation (SPO) rose maps were created by plotting the orientations of the long axes of the best-fit ellipse of each grain. The grain orientation spreads (GOSs), which are the proxies for dislocation density, were mapped to quantify the intracrystalline deformation.

**3. Seismic properties calculations.** the seismic properties of amphibole were computed using the MTEX tool (<https://mtex-toolbox.github.io>) based on the measured CPOs data, single-crystal elastic constants, the Christoffel equation and the Voigt-Reuss-Hill averaging scheme (Almqvist and Mainprice, 2017). The elastic constants and densities of amphibole for the calculation of seismic properties were chosen from Brown and Abramson (2016) according to the chemical compositions of amphibole in the studies samples (see Matlab script).

**Matlab script:**

```
%CPO and seismic properties calculation
[grains,ebsd.grainId] = calcGrains(ebsd);
% ebsd(grains(grains.grainSize<10)) = [];
[grains,ebsd.grainId] = calcGrains(ebsd,'angel','10*degree');
%One Point per Grain, for Pole Figure Analysis
OnePointPerGrains_amp = grains('Amphibole').meanOrientation;
odf_amp = calcDensity(OnePointPerGrains_amp,'halfwidth',10*degree);
OnePointPerGrains_feld = grains('Feldspar').meanOrientation;
odf_feld = calcDensity(OnePointPerGrains_feld,'halfwidth',10*degree);
% the fixed crystal directions
PF1AMP1 = Miller(1,1,0,ebsd('Amphibole').CS,'hkl');
PF1AMP2 = Miller(1,0,0,ebsd('Amphibole').CS,'hkl');
PF1AMP3 = Miller(0,1,0,ebsd('Amphibole').CS,'hkl');
PF1AMP4 = Miller(0,0,1,ebsd('Amphibole').CS,'uvw');
PF1AMP5 = Miller(1,1,0,ebsd('Amphibole').CS,'uvw');
PF1AMP6 = Miller(1,-1,0,ebsd('Amphibole').CS,'uvw');
h = {PF1AMP1,PF1AMP2,PF1AMP3,PF1AMP4,PF1AMP5,PF1AMP6};
% Plot figures colorful
plotPDF(odf_amp,h,'lower','resolution',2*degree,'contourf');
CLim(gcf,'equal');
mtexColorbar
%%Fabric Strength - Jindex and Mindex
Jindex= textureindex(odf_amp);
Mindex= calcMIndex(odf_amp);
% show the value of fabric strength
disp(' ')
disp(['Jindex = ',num2str(Jindex,3)])
disp(['Mindex = ',num2str(Mindex,3)])
disp(' ')
CS_amp = crystalSymmetry('12/m1', [9.9 18 5.4], [90,104.81,90]*degree, 'X||a*', 'Y||b*', 'Z||c',
'mineral', 'Amphibole', 'color', [0.58 0 0.83]);
rho_amp = 3.29;
C1ij = [[133.6 50.9 43.1 0 -0.8 0];...
[ 50.9 193.4 58.3 0 -10.8 0];...
[ 43.1 58.3 225.8 0 -30.3 0];...
[ 0 0 0 75.5 0 3.8];...
```

```

[ -0.8 -10.8 -30.3 0 47.5 0];...
[ 0 0 0 3.8 0 50.4]];
% define the tensor
C_amp = stiffnessTensor(Clij,CS_amp,'density',rho_amp);
[CVoigt_amp,CREuss_amp,CHill_amp] = mean(C_amp,odf_amp);
plotSeismicVelocities(CHill_amp)

```

## Reference Cited

- Almqvist, B. S. G., and Mainprice, D., 2017. Seismic properties and anisotropy of the continental crust: Predictions based on mineral texture and rock microstructure: *Reviews of Geophysics*, v, 55, p, 367–433.
- Bachmann, F., Hielscher, R., and Schaeben, H., 2010. Texture Analysis with MTEX – Free and Open Source Software Toolbox: *Solid State Phenomena*, v, 160, p, 63–68.
- Brown, J. M., and Abramson, E. H., 2016. Elasticity of calcium and calcium-sodium amphiboles: *Physics of the Earth and Planetary Interiors*, v, 261, p, 161171.
- Hielscher, R., and Schaeben, H., 2008. A novel pole figure inversion method: Specification of the MTEX algorithm: *Journal of Applied Crystallography*, v, 41, p, 1024–1037.
- Liao, Y., Wei, C, and Rehman, H. U., 2021. Titanium in calcium amphibole: Behavior and thermometry: *American Mineralogist*, v, 106(2), p, 180-191.
- Lloyd, G. E., Farmer, A. B., and Mainprice, D., 1997. Misorientation analysis and the formation and orientation of subgrain and grain boundaries: *Tectonophysics*, v, 279, p, 55–78.
- Mainprice, D., Bachmann, F., Hielscher, R., and Schaeben, H., 2014. Descriptive tools for the analysis of texture projects with large datasets using MTEX: strength, symmetry and components: *Geological Society Special Publications*, v, 409, p, 251–271.

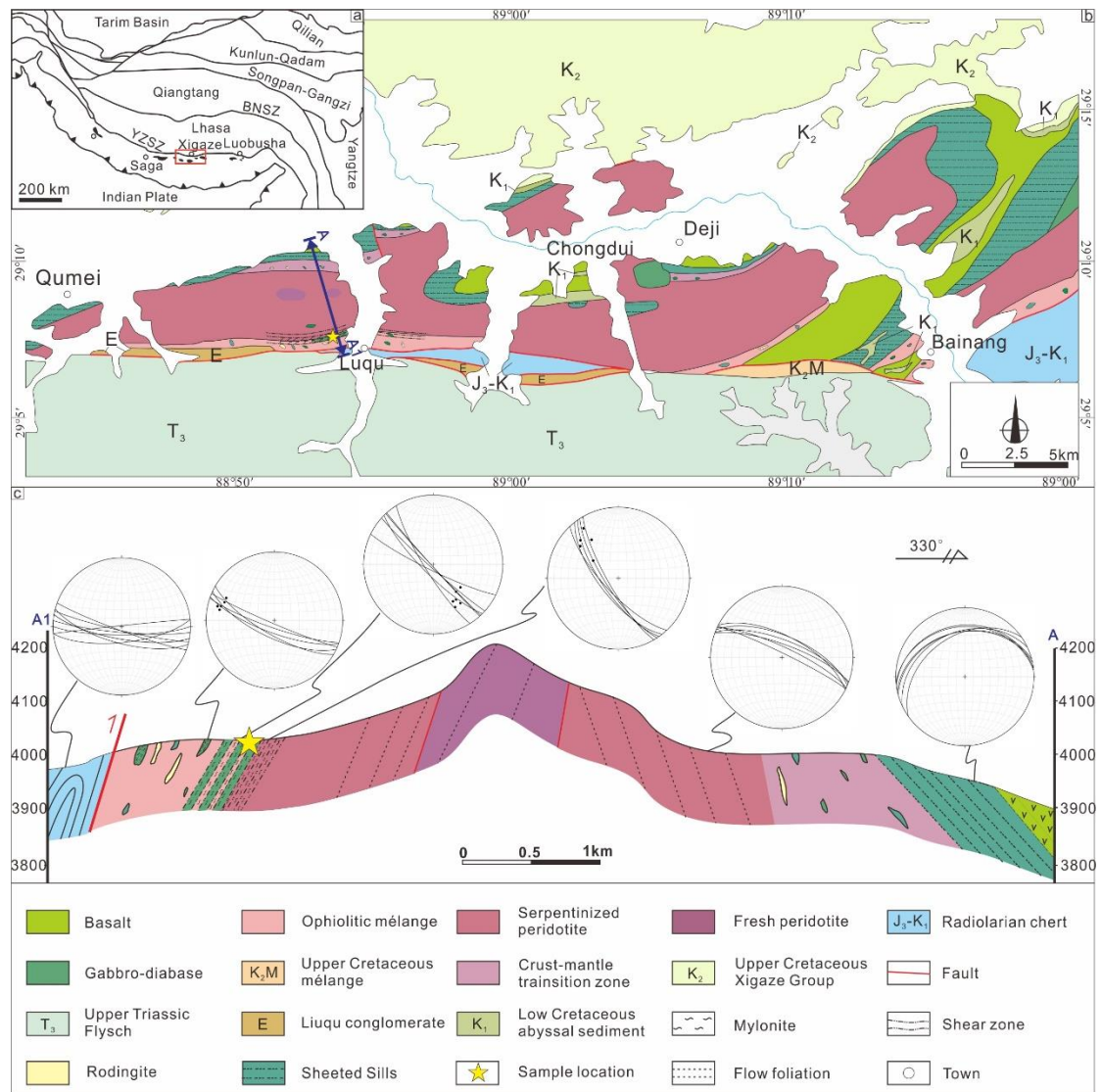


Fig. S1. (a) Simplified tectonic map showing the location of Xigaze ophiolite in the Tibetan-Himalayan Suture zone (red rectangle); YZSZ, Yarlung-Tsangbo suture zone; BNSZ, Bangong-Nujiang suture zone; (b) Geological map of the Xigaze area with the locations of samples and cross-section marked; (c) Schematic profile of the Luqu cross section and stereoplot of main fabric directions, lower-hemisphere equal-area.



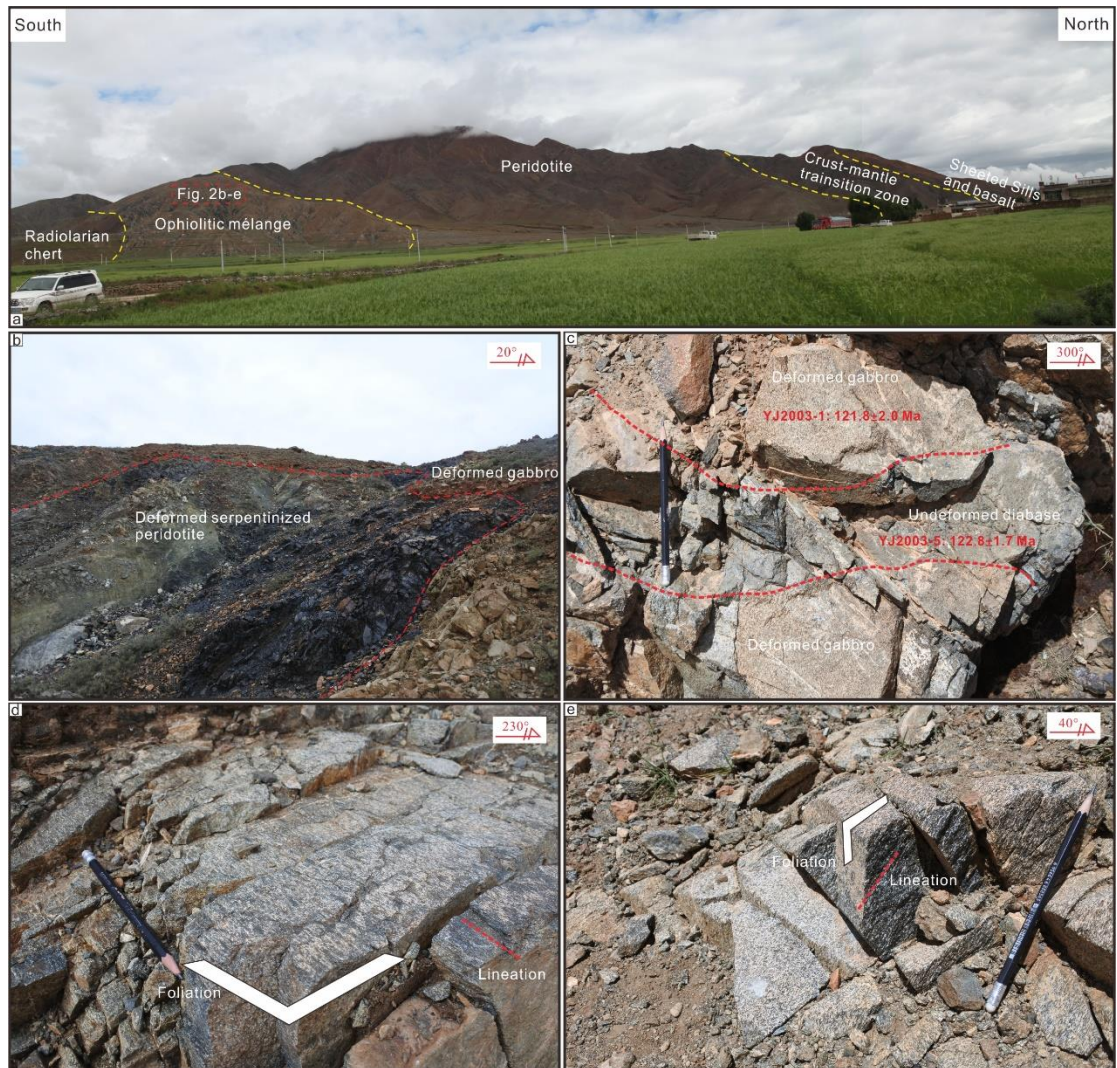


Fig. S2. Field photos of the discrete high-temperature shear zones in Luqu cross section. (a) The overall photo showing the main rock units in Luqu cross section; (b) The boundary between deformed gabbro and deformed serpentinized peridotite; (c) Sheared gabbro (YJ2003-1:  $121.8 \pm 2.0$ ) cut by undeformed diabase (YJ2003-5:  $122.8 \pm 1.7$  Ma); (d) and (e) Close-up photos of sheared gabbro showing the development of strong foliation and lineation.

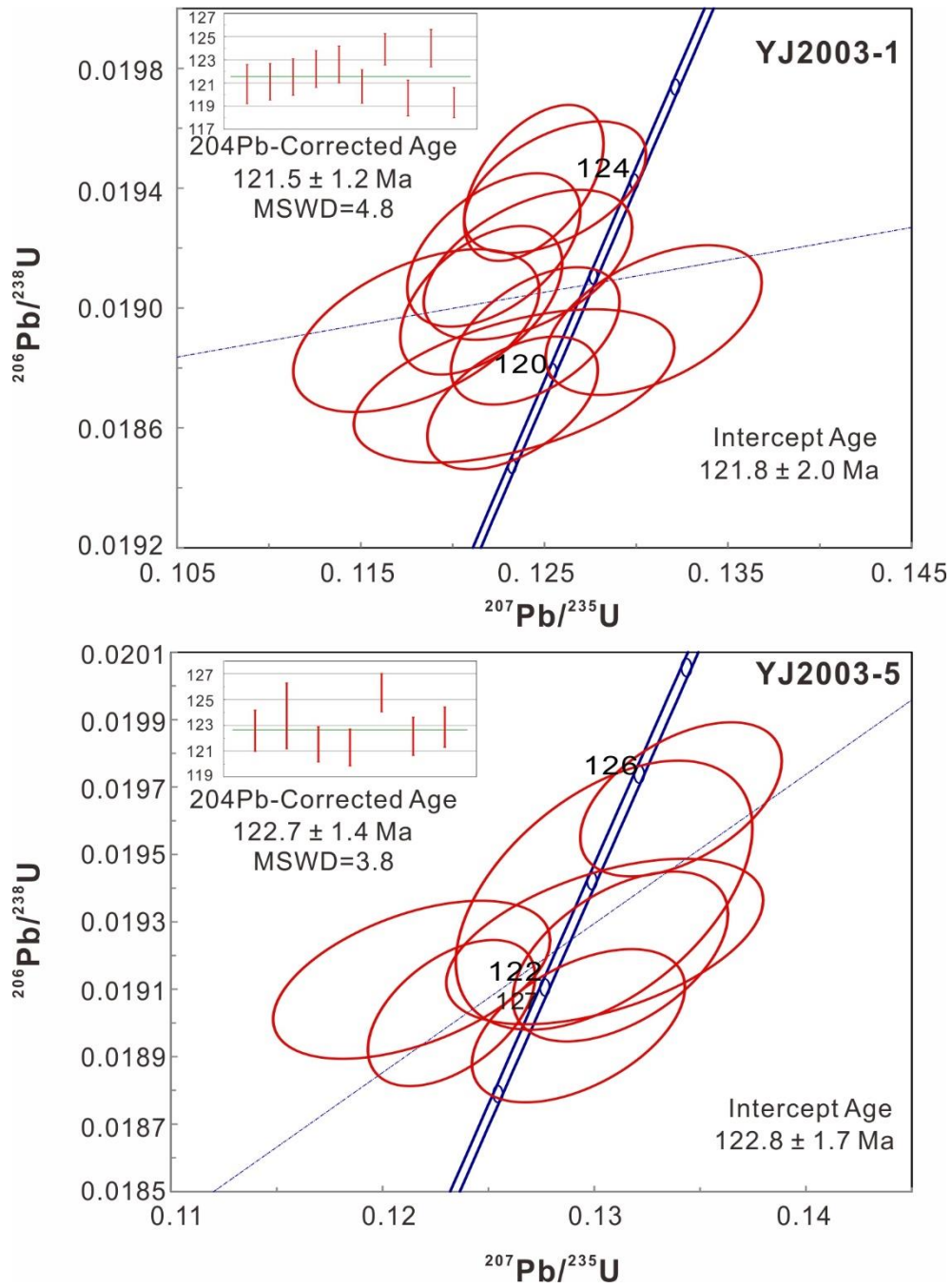


Fig. S3. SHRIMP Zircon U-Pb Concordia diagrams for (a) sheared gabbro (YJ2003-1) and (b) undeformed diabase (YJ2003-5). MSWD—mean square of weighted deviates.



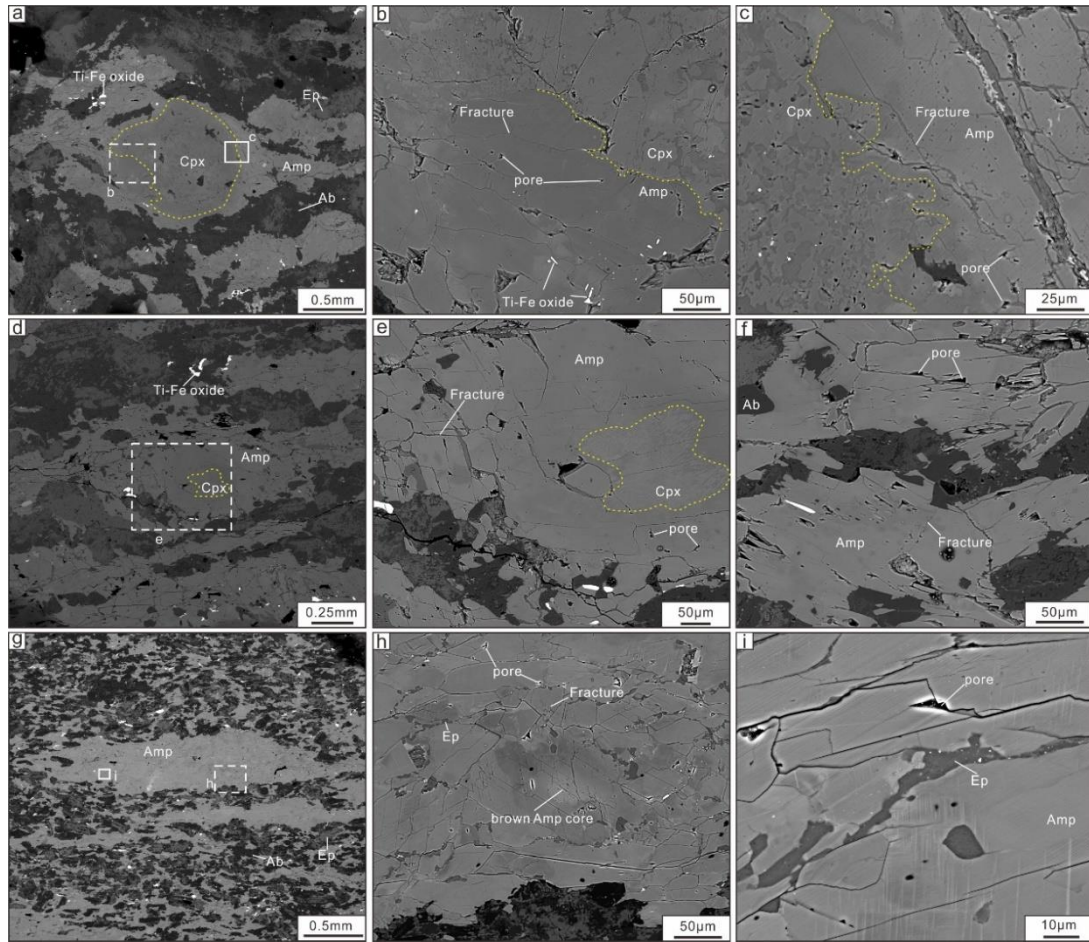


Fig. S4. Back-scattered electron (BSE) images showing the details of the microstructures in (a-c) type 1, (d-f) type 2 and (g-i) type 3 samples. (a-f) Widely distributed fractures and pores in amphibole, especially along the boundaries between amphibole and clinopyroxene; (g-h) Brown (high-Ti) amphibole core mantled by green (low-Ti) amphibole; (i) Epidote veins filling grain boundaries and fractures in amphibole aggregates. Amp, amphibole; Ab: albite; Cpx: clinopyroxene; Prh: prehnite; Ep: epidote.

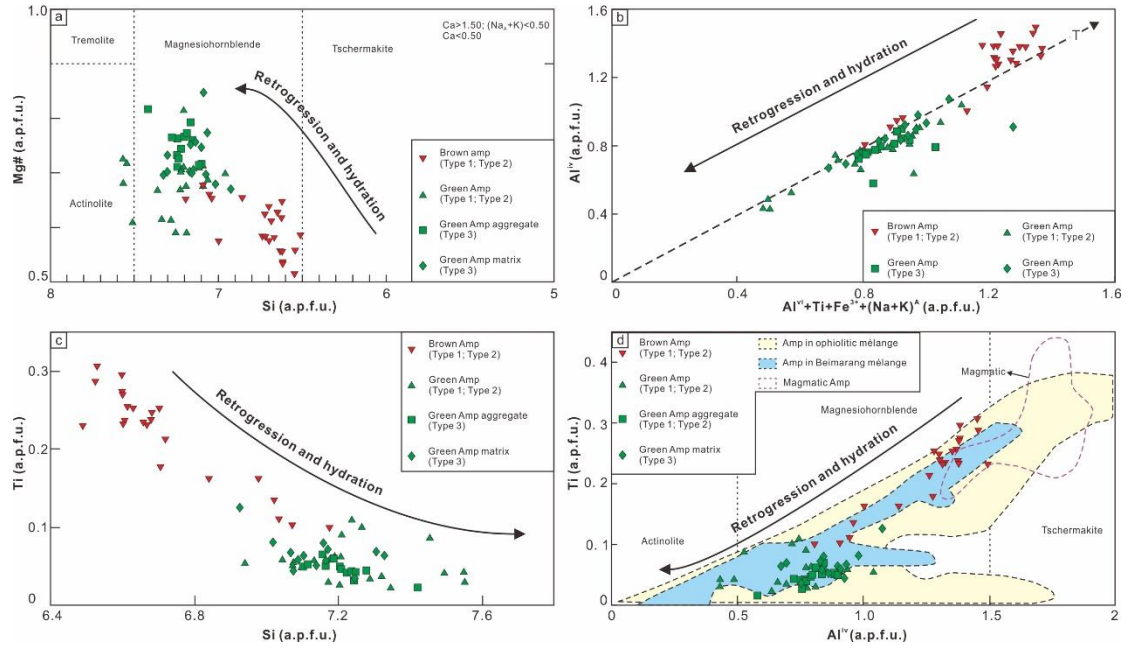


Fig. S5. Point analysis and compositions for amphibole. (a) Diagram of classification of calcic amphibole after [Leake et al. \(1997\)](#); (b) Diagram of  $Al^{IV}$  vs.  $Al^{VI} + Ti + Fe^{3+} + (Na+K)^A$  plot. Increasing values along this line indicates increasing temperature; (c) Diagram of Ti vs. Si plot; (d) Diagram of Ti vs.  $Al^{IV}$  plot. Fields for ‘ophiolitic mélange’ (yellow region) and ‘Beimarang mélange’ (cyan region) are from [Dupuis et al. \(2005\)](#) and [Huot et al. \(2002\)](#), respectively. Fields for ‘Magmatic Amp’ is from [Coogan et al. \(2001\)](#).



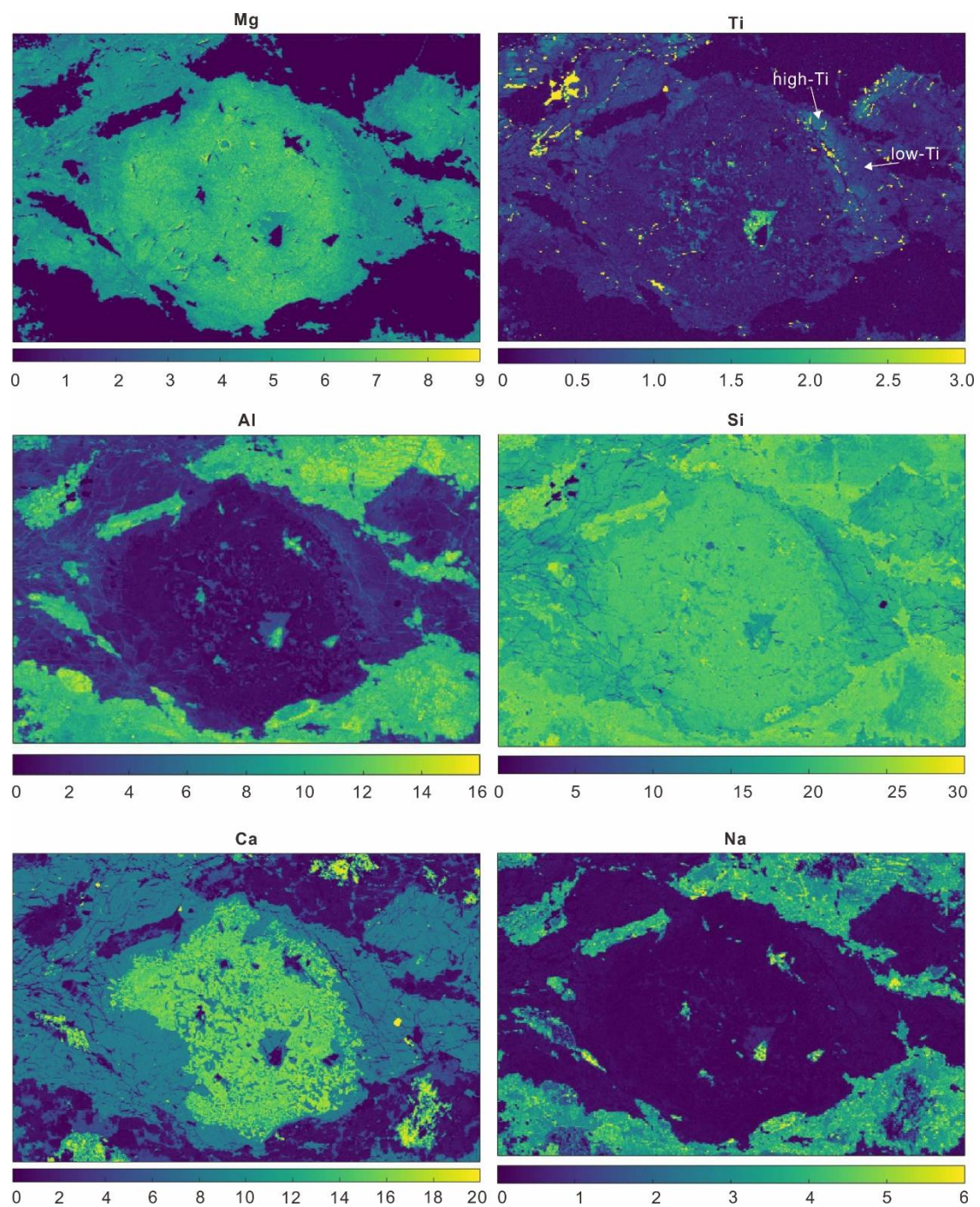


Fig. S6. Element maps for clinopyroxene and amphibole grains in the region of Figure 1b (type 1 sample; YJ2008-2) showing the compositional zoning of amphibole porphyroclast.

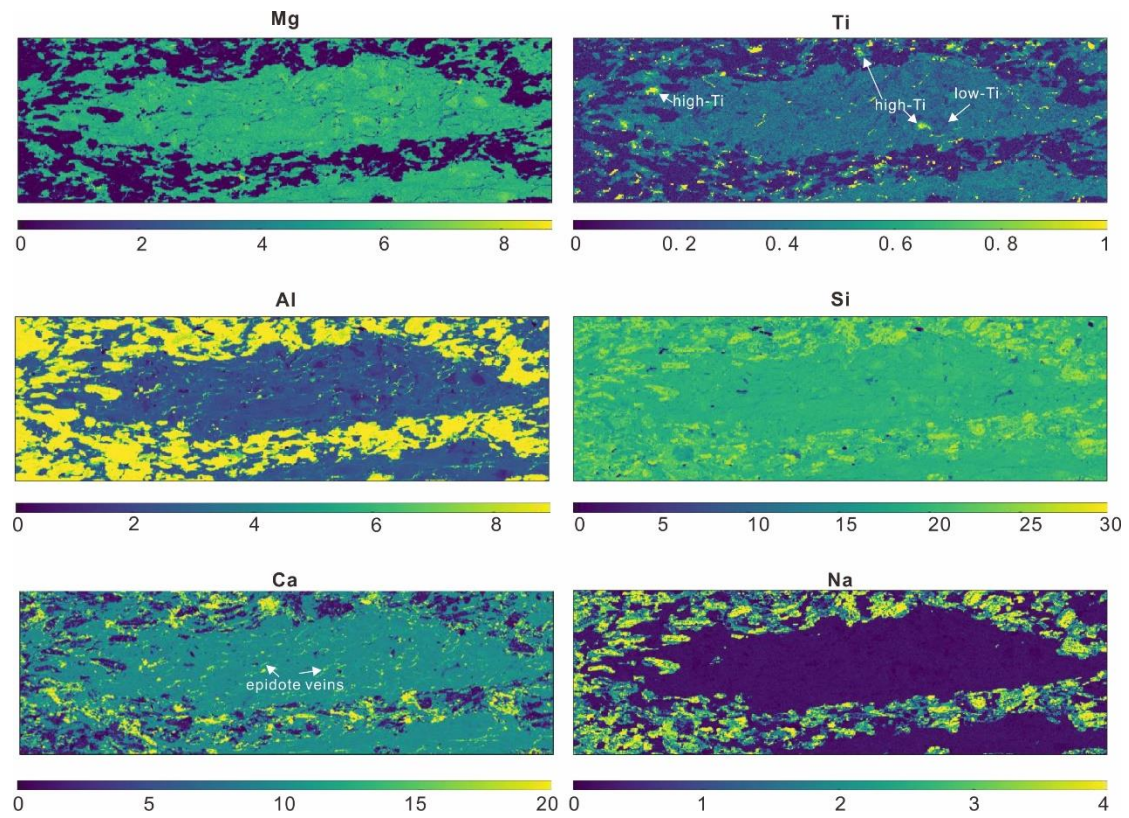


Fig. S7. Element maps for amphibole aggregates in type 3 samples (YJ2010-1) showing the existence of (1) high-Ti amphibole core in amphibole aggregates and matrix and (2) fine epidote veins distributed within the grain boundaries of amphibole aggregates.



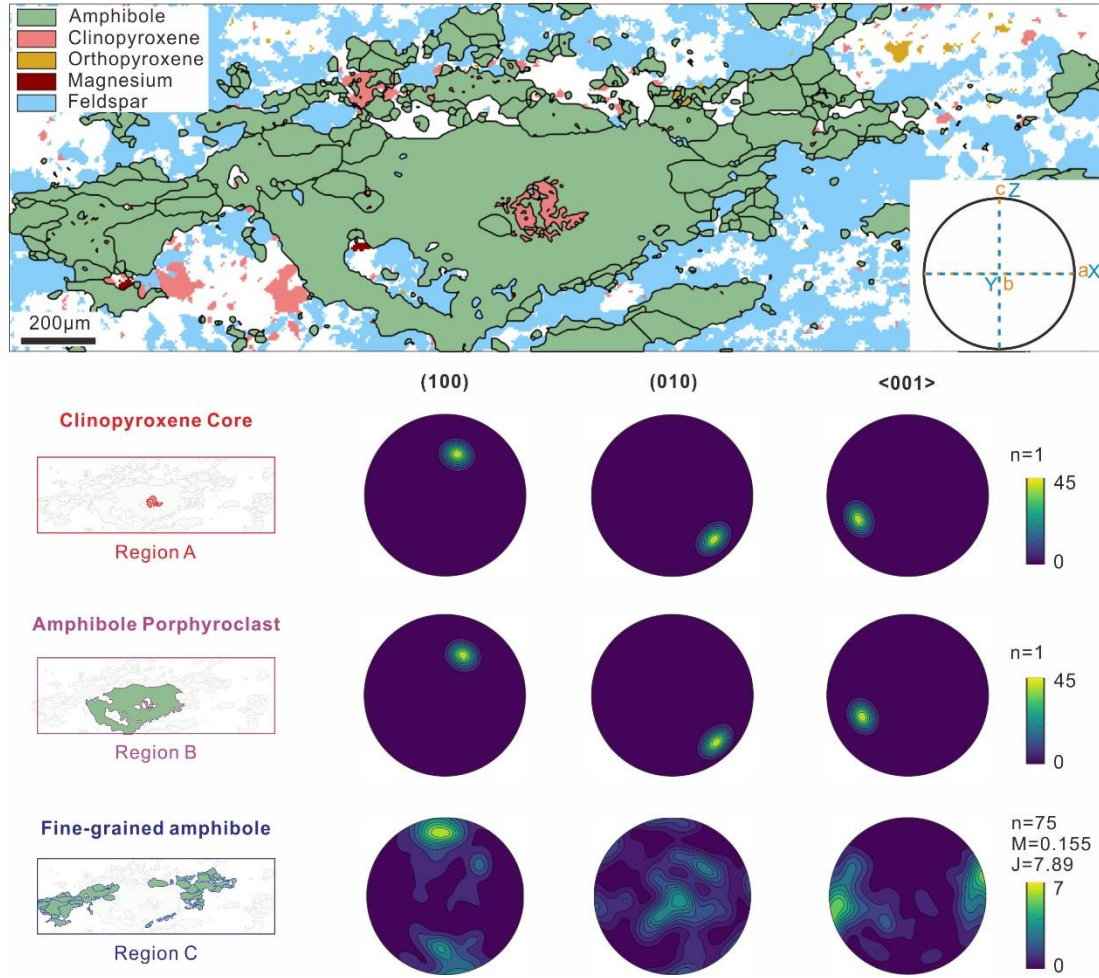


Fig. S8. Detailed CPO analysis of clinopyroxene and amphibole grains in a type 2 sample (YJ2003-1). Region A (red) is the clinopyroxene core. Region B (purple) is the amphibole porphyroclast. Region C (green) includes most of the surrounding amphibole matrix. M: M-index; J: J-index; n: number of measured grains.

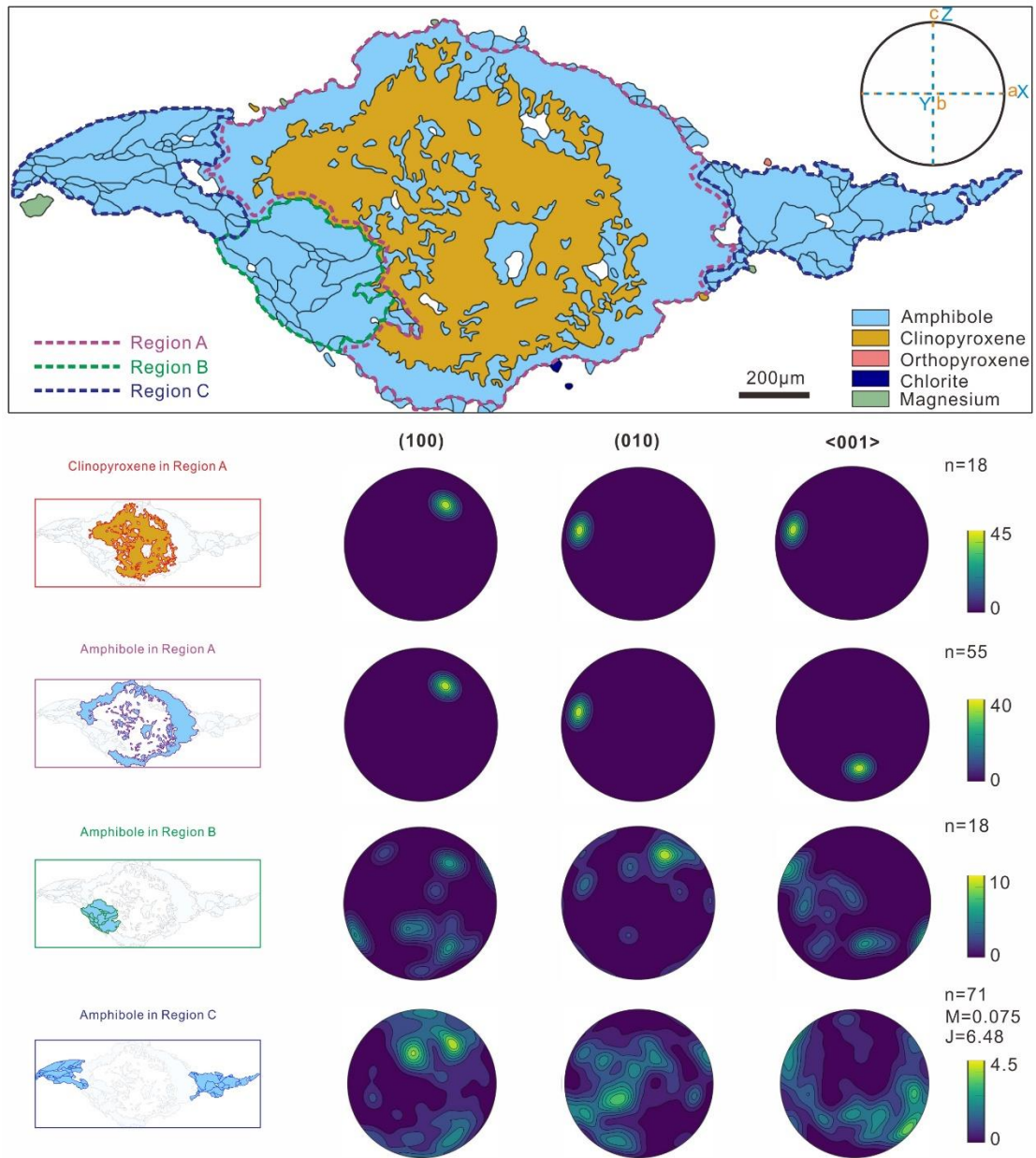


Fig. S9. Detailed crystal preferred orientation (CPO) analysis of clinopyroxene and amphibole grains in a type 1 sample (YJ2008-2). Region A (red) is the clinopyroxene core. Region B (purple) is the amphibole porphyroclast. Region C (green) contains amphibole matrix in the direction oblique to lineation. Region D (blue) focuses on the amphibole matrix in strain shadow. M: M-index; J: J-index; n: number of measured grains.



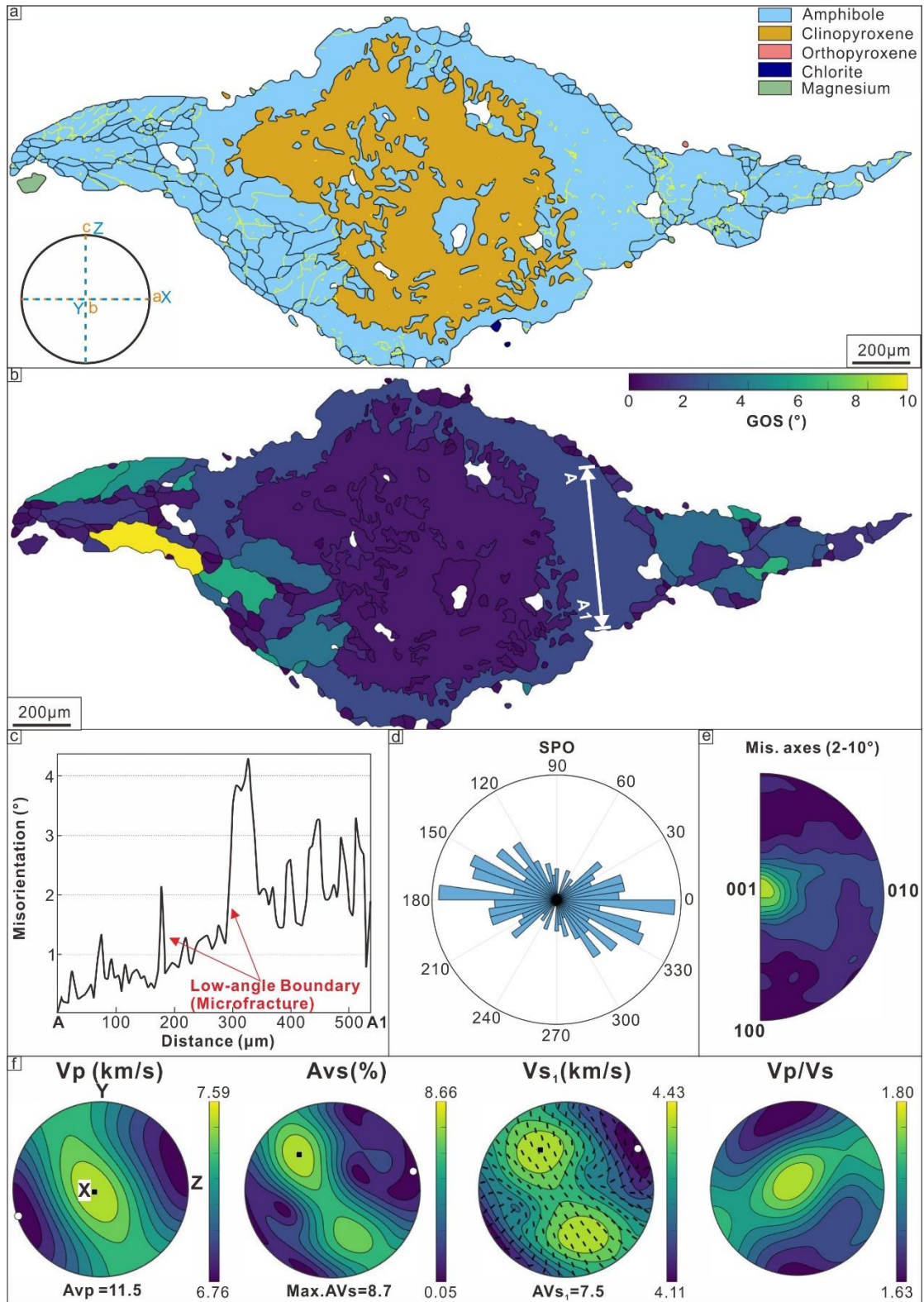


Fig. S10. EBSD mapping results and calculated seismic properties of amphibole in a type 1 sample (YJ2008-2). (a) Phase map with low-angle grain boundaries ( $<10^{\circ}$ ; yellow lines) plotted; (b) Grain orientation spread (GOS) map showing GOS values in

clinopyroxene and amphibole grains; (c) Misorientation profile showing the misorientation changes cross the amphibole porphyroclast; (d) Shape preferred orientation (SPO) rose diagram of amphibole grains; (e) Inverse pole figures showing the distribution of correlated misorientation axes (between 2 and 10°); (f) Calculated seismic properties ( $V_p$ ,  $AV_s$ ,  $V_{s1}$  and  $V_p/V_s$ ) of amphibole.

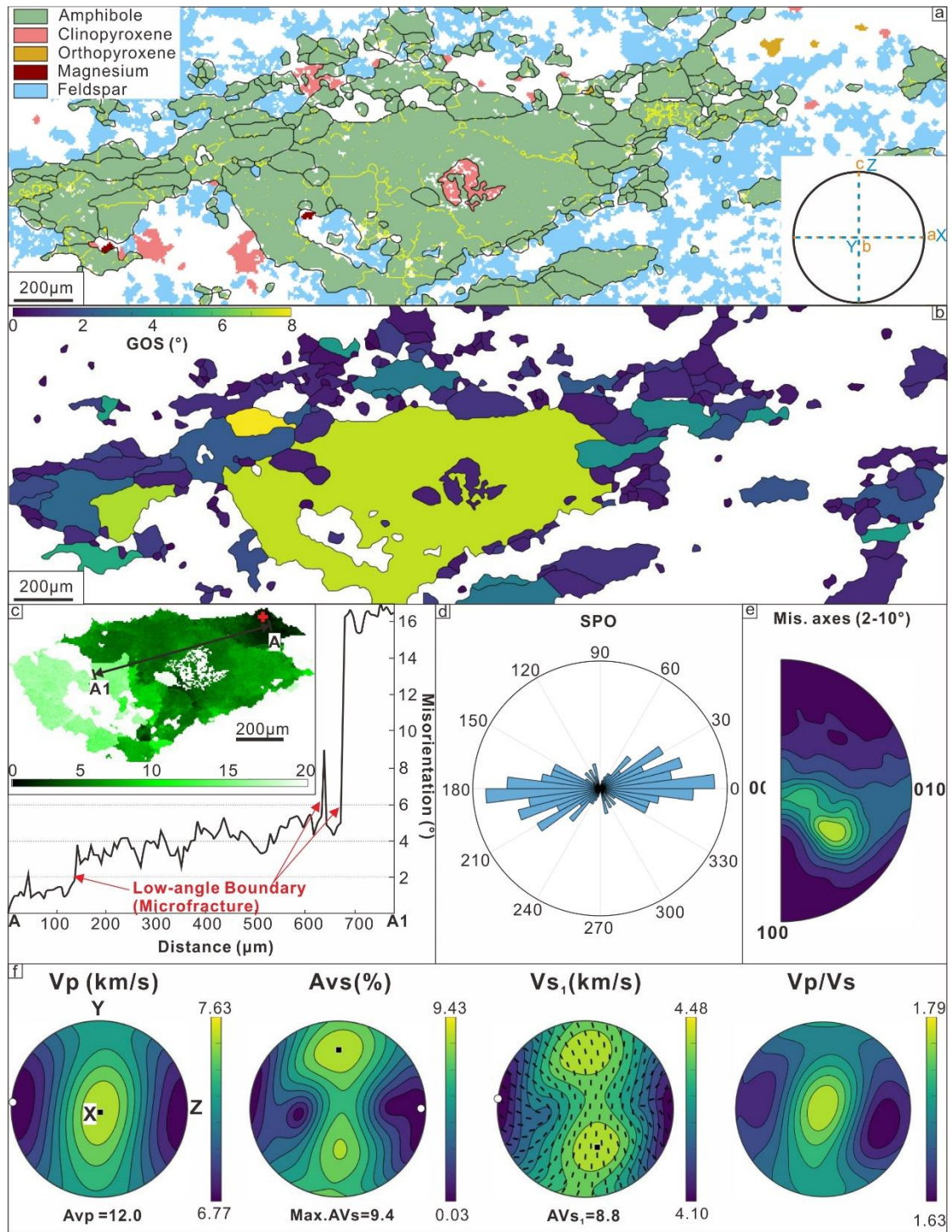


Fig. S11. EBSD mapping results and calculated seismic properties of amphibole in type 2 samples (YJ2003-1). (a) Phase map with low-angle grain boundaries plotted ( $<10^\circ$ ; yellow lines); (b) GOS map showing GOS values in clinopyroxene and most amphibole grains; (c) Texture component map (TCM) of amphibole porphyroclast showing the misorientation from the reference point marked by the red cross and misorientation profile across amphibole porphyroclast; (d) SPO rose diagram; (e)

Inverse pole figures showing the distribution of correlated misorientation axes (between 2 and 10°);

(f) Calculated seismic properties ( $V_p$ ,  $AV_s$ ,  $V_{s1}$  and  $V_p/V_s$ ) of amphibole.



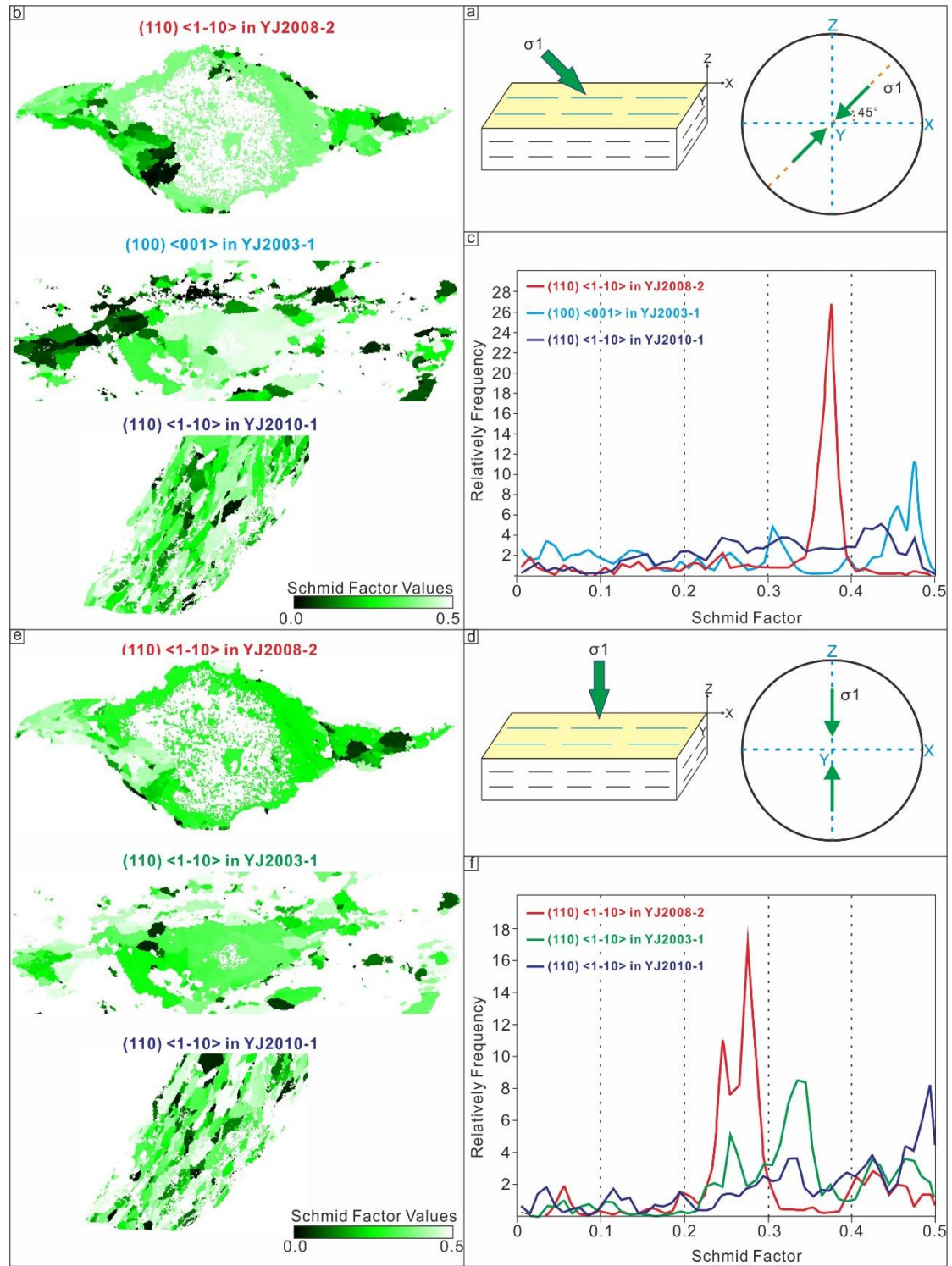


Fig. S12. Schmid factor analysis for amphibole in type 1–3 samples under (a–c) general shearing and (d–f) pure shearing. (a and d) The cartoons showing compression direction relative to the kinematic reference frame; (b and e) Schmid factor map colored according to Schmid factor of the slip systems with the maximum integrated Schmid factor for type 1–3 samples; (c and f) Relative

frequency of Schmid factor values of the slip systems with the maximum integrated Schmid factor  
for type 1–3 samples.

## Reference cited

- Coogan, L.A., Wilson, R.N., Gillis, K.M., and MacLeod, C. J., 2001. Near-solidus evolution of oceanic gabbros: Insights from amphibole geochemistry: *Geochimica et Cosmochimica Acta*, v, 65, p, 4339–4357.
- Dupuis, C., Hébert, R., Dubois-Côté, V., Wang, C.S., Li, Y.L., Li, Z.J. Petrology and geochemistry of mafic rocks from mélange and flysch units adjacent to the Yarlung Zangbo Suture Zone, Southern Tibet: *Chemical Geology*, v, 214, p, 287–308.
- Huot, F., Hébert, R., Varfalvy, V., Beaudoin, G., Wang, C., Liu, Z., Cotton, J., Dostal, J. The Beimarang mélange (southern Tibet) brings additional constraints in assessing the origin, metamorphic evolution and obduction processes of the Yarlung Zangbo ophiolite: *Journal of Asian Earth Sciences*, v, 21, p, 307-322.
- Leake, B.E., Woolley, A.R., Arps, C.E.S., Birch, W.D., Gilbert, M.C., Grice, J.D., et al., 1997. Nomenclature of amphiboles: Report of the subcommittee on amphiboles of the international mineralogical association, commission on new minerals and mineral names: *American Mineralogist*, v, 82, p, 1019–1037.